SUPPORTING MATERIAL

Copper-Based Pulsed Dipolar ESR Spectroscopy as a Probe of Protein Conformation Linked to Disease States

Gregory E. Merz, Peter P. Borbat[a], AshleyJ. Pratt[†], Elizabeth D. Getzoff[†], Jack H. Freed[a]* and Brian R. Crane*

Department of Chemistry and Chemical Biology, Cornell University, Ithaca, NY 14850
[a]National Biomedical Center for Advanced ESR Technology (ACERT), Cornell University.
[†]Department of Integrative Structural and Computational Biology, The Scripps Research Institute, La Jolla CA 92037

Content

A. Structural Data

Fig. S1, Table S1

B. Pulse Dipolar ESR Spectroscopy

B.1. Methods

Fig. S2

B.2. PDS Data Collection

Fig. S3

B.3. Orientational Effects

Fig. S4

B.4 Supplemental PDS Data

Figs. S5-S10

C. Structural Modeling and Assessment of SOD1 Aggregation

Figs. S11-S13

Supporting References

A. Structural Data

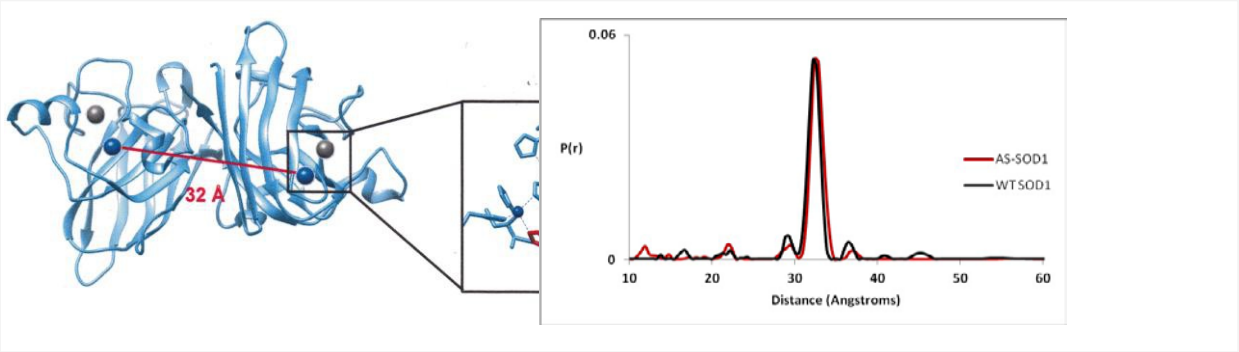

Figure S1. (Left) Crystal structure of human SOD1 (PDB ID: 2V0A). 32 Å separate the copper ions across the dimer interface (blue). Zinc ions (grey) reside beside the copper ions. Inset shows the active site metal coordination environment, with the histidine 48 side chain shown in red. Variant H48Q, for which Cu-Cu distance is 34 Å (See Figure 2, main text), substitutes a ligand to Cu^{2+}.

(Right) Cu-Cu distance distributions for WT SOD1 vs. its C6A:C111S mutant, (abbreviated as AS-SOD1) reconstructed with the L-curve Tikhonov regularization method and refined using the Maximum Entropy Method (MEM).

Table S1. Crystallographic data collection and refinement statistics.

Data Collection Metrics	
Space Group	$C222_1$
Unit Cell Dimensions, (Å)	a = 165.10
	b = 203.81
	c = 144.41
Unique Reflections	95,238
Resolution, (Å)	36.10-2.38
Last Shell, (Å)	2.44-2.38
Redundancy, (%/last shell)	6.4/2.9
Completeness, (%/last shell)	98.35/79.40
I/σ, (overall/last shell)	10.9/1.52
Linear R-fac (R_{merge}), (overall/last shell)	0.209/0.714
CC ½ (overall/last shell)	0.973/0.543
Refinement Metrics	
R-Work, (%/last shell)	0.166/0.225
R-Free, (%/last shell)	0.215/0.290
No. atoms	22,063
No. water molecules	891
Mean B value	21.9
RMSD from ideal bond lengths, (Å)	0.014
RMSD from ideal bond angles, (Å)	1.4

B. Pulse Dipolar ESR Spectroscopy

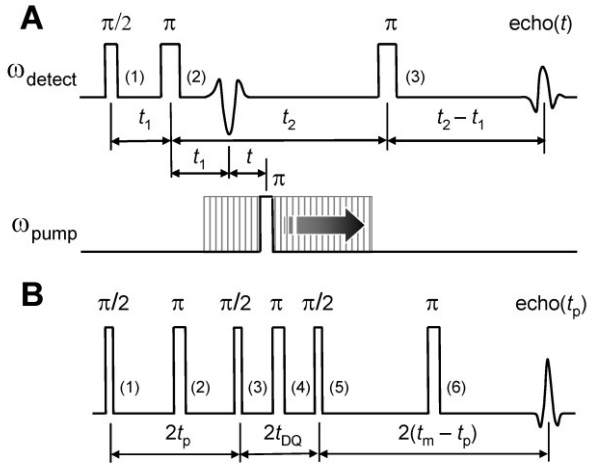

B.1. *Methods*

Figure S2. (**A**) The 4-pulse DEER and (**B**) the 6-pulse DQC PDS pulse sequences. Both pulse sequences shown in Fig. S2 are well described in the literature (1, 2). Briefly, in the (4-pulse) DEER method (3) a refocused primary echo is created by the sequence of mw pulses 1, 2, and 3, $\pi/2–t_1–\pi–t_2–\pi–(t_2 - t_1)–$echo applied at the frequency ω_{detect}, thus selecting for detection of the electron spins at the desired field position, while the "pump" π-pulse is applied at sufficiently different frequency, $\omega_{pump.}$ Hence it flips the electron spins corresponding to a different part of the ESR spectrum. The time position of the pump pulse is advanced in small steps from the 2nd to the 3rd detection pulse, producing an amplitude modulation of the echo. The modulation pattern thus mainly represents the "dipolar" oscillations from the dipole-dipole interaction between the electron spins. From the oscillation frequency, $\omega_{dip} \propto 1/r^3$ the distance, r could be accurately determined. The position of the echo does not change in this version of DEER, therefore variable relaxation and nuclear ESEEM contributions to the echo amplitude are relatively small. In the 6-pulse DQC sequence, based on intense mw pulses applied at a single frequency, pulses 2 to 6

move in such a manner that position of the echo also does not change. Pulses 3, 4, and 5 move as a group, while refocusing π-pulses, 2 and 6 are always in the middle of respective intervals "$2t_p$" and "$2t_m - 2t_p$". Dipolar oscillations recorded as a function of $t_\xi \equiv t_m - 2t_p$ are separated from other contributions to the echo by phase cycling.

B.2. ***PDS Data Collection***

Four-pulse DEER (Fig. S2) of SOD1 was carried out on a modified home-built Ku-band, FT ESR spectrometer (4) operating over the 17.0-17.6 GHz frequency range and optimized for PDS (5). The measurements were carried out on 80-350 μM SOD1, (Tris-buffered saline and 30% glycerol, the buffer was deuterated in some samples, as noted) at 15-20 K for Cu-Cu and Cu-NO detection, and 20-30 K for NO-NO detection using a CF935 flow-cryostat with ITC503A temperature controller (Oxford Instruments, Inc.). Fig. S3 shows in (A) the field-swept echo-detected ESR spectrum recorded at 15 K at a pulse sequence repetition rate of 4 kHz. At this rate, the otherwise dominant, R1 spectrum was attenuated by a large factor, making the Cu^{2+} spectrum appear more intense. The broad extent (~1000 G) of the Cu^{2+} ESR spectrum permits a wider separation between the pump and detection frequencies (limited by resonator bandwidth) and hence increased pulse intensities than those applied with nitroxides. For DEER detection on Cu^{2+} we typically used an 8/16/16 ns π/2-π-π pulse sequence, while a 16/32/32 ns were used for nitroxides. The pump pulse in these cases was 8 ns for Cu-Cu but was limited to 16 ns for Cu-NO in order to keep non-linear effects caused by simultaneous flipping of two NO spins small, even though it was possible to flip more than 50% of the spins by using an 8 ns or shorter pumping pulse. The spectral positions selected for pump and detection are denoted by arrows in Fig. S3.

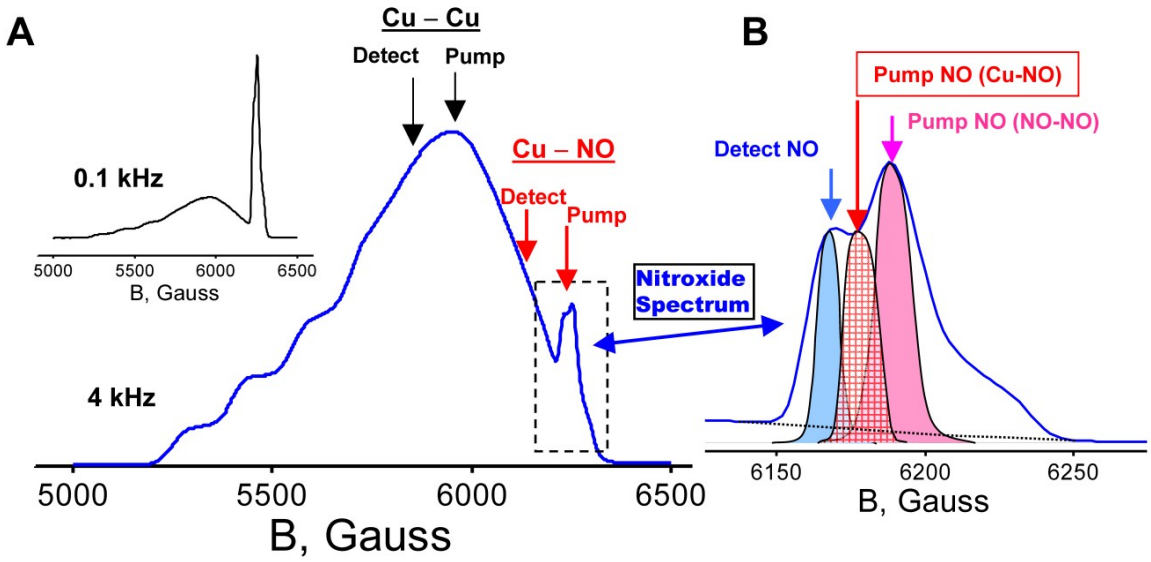

Figure S3. (**A**) Field-swept echo-detected SOD1 Cu^{2+} ESR spectrum was recorded at 15 K and 4 kHz repetition rate. On the high-field side the spectrum from nitroxide labels is visible. The arrows indicate spectral positions of detection and pumping used in these set of measurements. The inset on the left was recorded at low repetition rate and is dominated by the narrow nitroxide spectrum. (**B**) The nitroxide field-sweep echo-detected spectrum is plotted on expanded field scale to show more clearly the positions of spectral excitations. The spectrum was recorded at 30 K and 0.5 kHz repetition rate. NO-NO DEER data were obtained in the standard manner, as shown. The temperature range used was 20-30 K, with the optimum being at 30 K.

B.3. ***Orientation Correlation Considerations***

The Cu^{2+} magnetic tensor principal axis system of bovine SOD (6) has g_z moderately tilted away from the inter-copper vector (**u),** which could introduce orientation correlation effects with respect to g_z but not for the $g_{x,y}$ spectral regions. Moreover, inhomogeneous hyperfine broadening comparable to the difference between the pump and detection frequencies further randomizes orientational effects over the $g_{x,y}$, region. Thus, due to the stronger orientational correlations at g_z, the g_z spectral region was avoided. Fortunately, reconstruction artifacts caused by reduced contributions at g_z are expected to be minimal because the orientations selected at g_z have **u** aligned parallel to the static magnetic field and orientations of **u** less than the magic angle do not contribute substantially in the Tikhonov treatment. As expected, the DEER data recorded at g_x and g_y were nearly identical (see Fig. S4 below) and distance reconstruction exhibited few spurs. It is important to note that this simplification may not be appropriate for other copper systems: for example, one with an axial *g*-tensor that has *z* perpendicular to **u.** For such a case, orientational effects will likely necessitate a more complicated distance analysis, with related examples known for nitroxides (7).

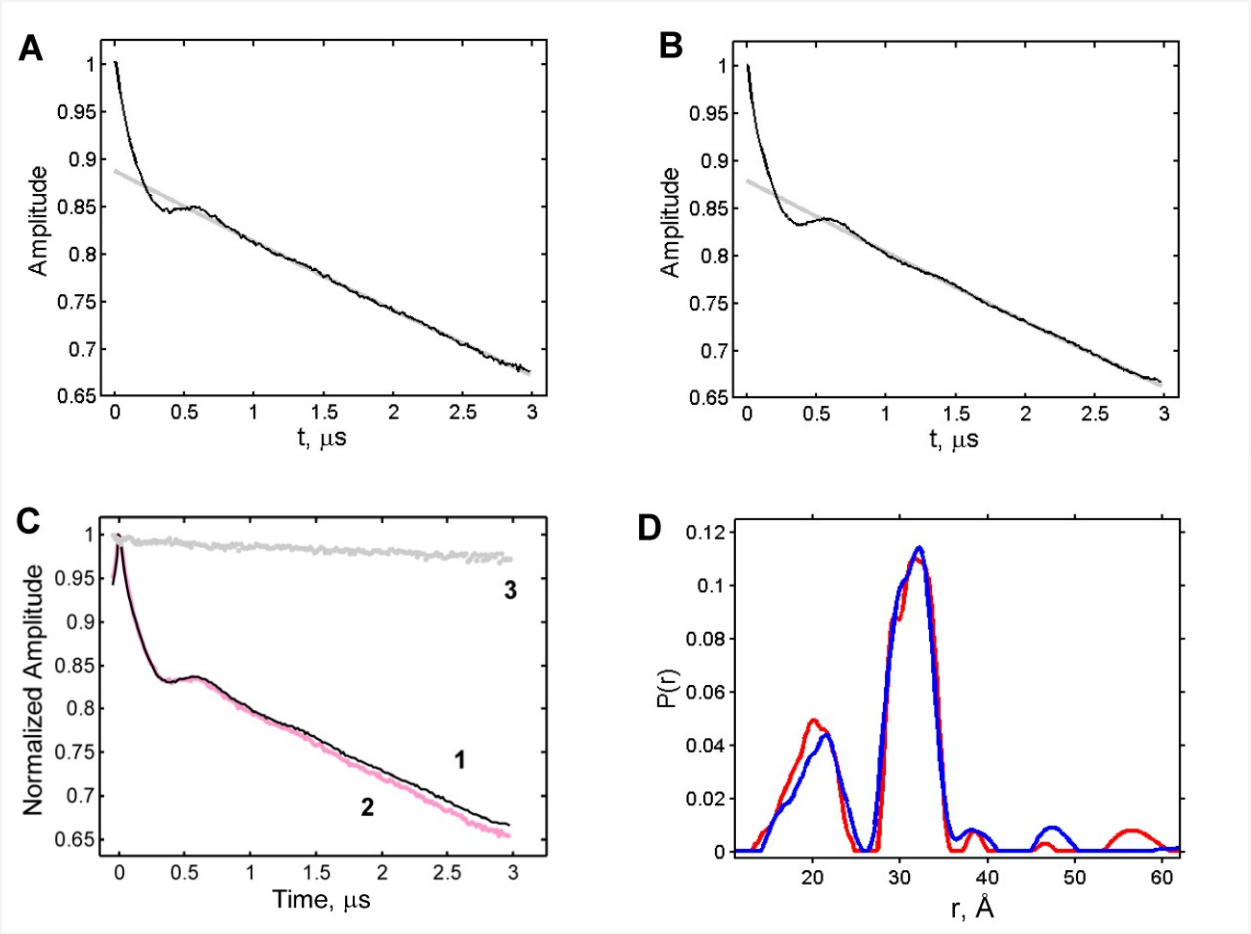

Figure S4. (**A, B**) Raw Cu-Cu time-domain data are shown for 350 μM 1 V94R1:I149T mutant of AS-SOD1 for detection centered at g_y and g_x, (A and B, respectively). Pumping frequency was applied at g_y spectral maximum. Modulations depths are ≈0.011 in A and ≈0.012 in B. (**C**) The data from panels A and B were adjusted to the same modulation depth by subtracting a small constant value from B before normalizing to unity at zero time. In panel C, (1) and (2) correspond to B and A. Here, (3) is the ratio of (2) to (1) showing a very small change in the dipolar oscillations shape between two cases. (**D**) Distance distributions for A (red) and B (blue).

S3.4. *Supplemental PDS Data*

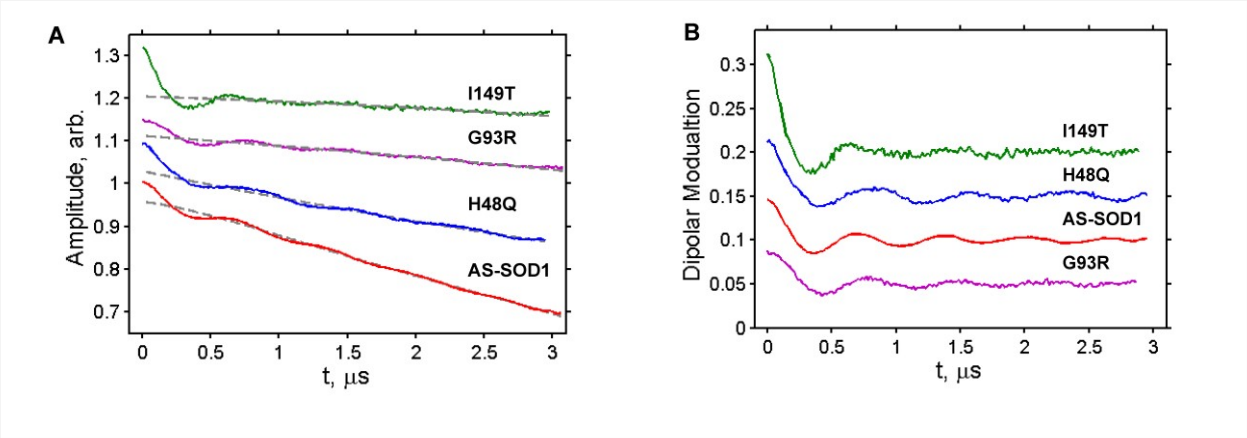

Figure S5. Examples of typical Ku-band 4-pulse DEER Cu-Cu data shown for the following SOD1 fALS mutants: I149T, G93R, H48Q, AS-SOD1. (**A**) Raw signals are plotted for these mutants with the baseline fits. (**B**) Pure dipolar oscillations after baseline removal from the data in A. The data in A and B were distributed vertically for clarity. The following conditions were used: pump pulse was 8 ns except H48Q that used 6 ns pulse. Detection pulses were 8 ns for $\pi/2$ pulse and 16 ns for π-pulses. The center maximum at g_y was used for pumping in all cases. The data were acquired at 15-20 K and 2 to 4 kHz pulse sequence repetition frequency. Data averaging times were ~13.5 h.

The short spin-lattice relaxation time, (T_1) of Cu^{2+} enables a repetition frequency of 2 to 4 kHz at the optimal temperature ~20 K, which in combination with the more intense pulses, partly offsets a low spectral intensity arising from wide Cu^{2+} ESR spectrum. Sufficiently long Cu^{2+} T_2's (~2.5 μs) permitted DEER recording up to 3 μs with good signal-to-noise (SNR) already after 2-8 hours of data averaging for the concentrations used. The longer time of 13.5 h was an outcome of overnight measurements. In right panel SNR is good for all data and is excellent for AS-SOD1, thus even less averaging time would be necessary in most cases.

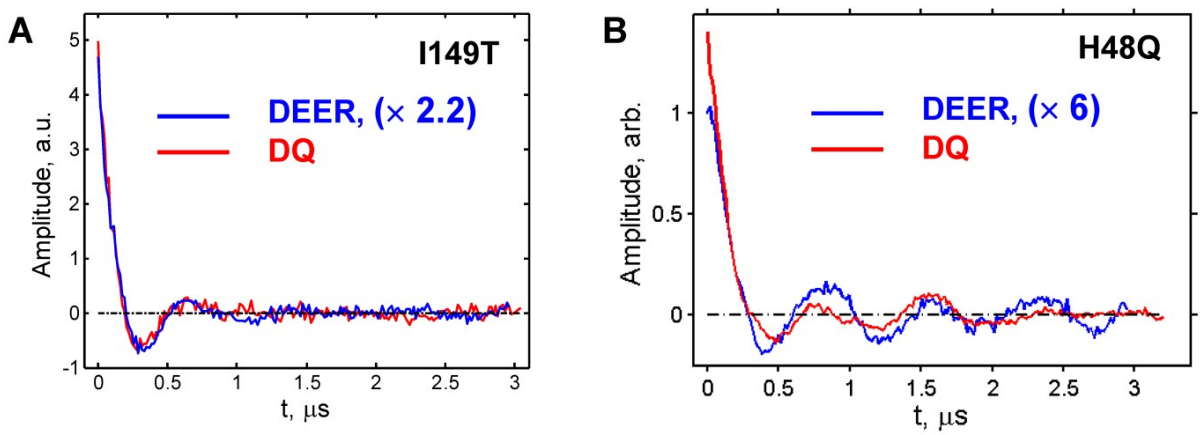

Figure S6. Ku-band DEER (blue) and DQC (red) for Cu^{2+}/Cu^{2+} pair of (**A**) I149T and (**B**) H48Q fALS mutants. The data are compared after subtracting backgrounds and scaling the result to similar amplitude of oscillations. In B, DEER was recorded in 13.4 h at 20 K using 6 ns pumping and 140 MHz frequency separation. DQC used π-pulses of 4 ns (B_1 ~45 G) and was recorded in 110 min at the same (g_y) field position and temperature. The dipolar signal in B is about 6-7 times stronger in DQC. In both cases (A and B) an order of magnitude shorter averaging time was needed for reaching the same SNR in DQC than in DEER.

A 4 ns pump π-pulse in our DQC experiments excited ~40 G extent of the Cu^{2+} spectrum. We note that a feasible doubling of this spectral extent would increase the SNR by a factor of 3-4. The main difficulty observed with DQC was the contribution of a broad range of low ESEEM frequencies from the four nitrogens of Cu^{2+}-coordinated histidine residues (8). However, when an experiment requires the detection limit, these complicating ESEEM are then generally at the level of noise. Note that the Cu-DQC tested in this work is utilized in its generic form (2, 9, 10), which is different from the variants reported elsewhere (8, 11). It should also be noted that in the Cu-Cu and Cu-NO measurements by DEER more intense pump and detection pulses could be applied, thereby extending the short-distance range down to ~15 Å and reducing the difference in SNR between the two methods.

We estimated the concentration sensitivity in Cu-Cu measurements is about 30% and for Cu-NO is about the same or potentially higher compared to typical 60 K NO-NO measurements on soluble proteins. NO-NO measurements were temperature-optimized (at 30 K) to tradeoff between a long T_1 at 20 K and a short T_2 at 60K caused by the fast-relaxing copper ion. In Cu-NO experiments, the pumping pulse was applied to the nitroxide due to its narrower spectrum and also to avoid a large reduction in detection efficiency due to a very long T_1 below 20 K. Although it is possible to flip a large percentage of the NO spins by using a 4-6 ns pump π-pulse, the pumping was limited to an 8 or 16 ns π-pulse width to minimize excitation overlap with Cu and non-linear multi-spin effects. This contrasts with the 6-pulse DQC experiment, wherein all the pulses are at the same frequency. DQC is not applicable to the Cu-NO case because of very small spectral overlap between Cu^{2+} and the nitroxide.

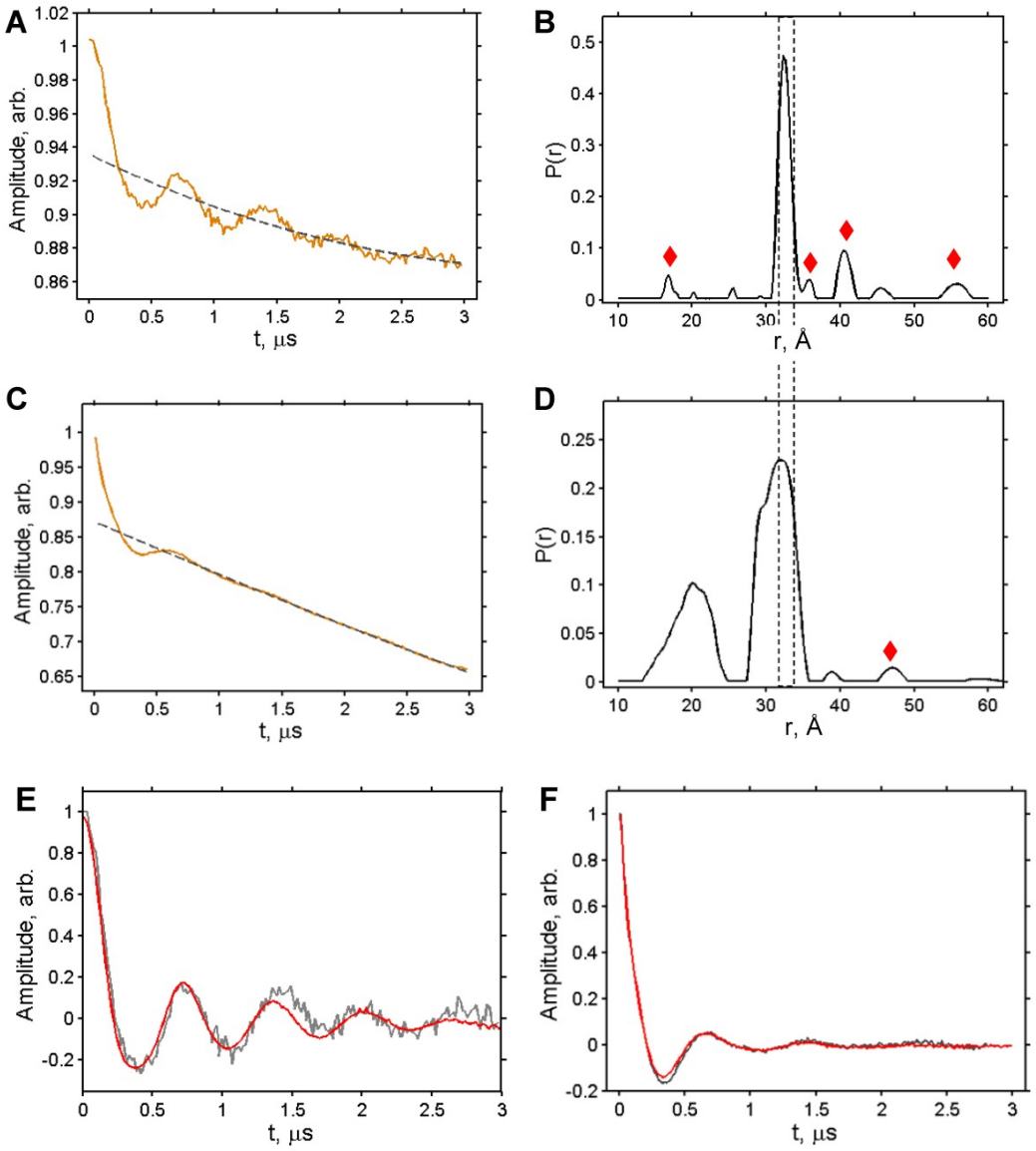

Figure S7. Raw time-domain DEER data from Cu-Cu experiment: Data in (**A**, **B**) are for 150 μM V94R1, whereas (**C**, **D**) is for 350 μM V94R1:I149T. There is stronger damping of oscillations in (C) due to apparently greater extent of disorder in this mutant. Also, the short-distance component and greatly increased modulation depth in (**D**) from ~0.06 to ~0.12 both point to the presence of aggregates in I149T. (**E**, **F**) Comparison of experimental data with the fits based on reconstructed $P(r)$. Diamonds in panels B and D indicate spurious non-reproducible peaks in $P(r)$; they were excluded in the fits.

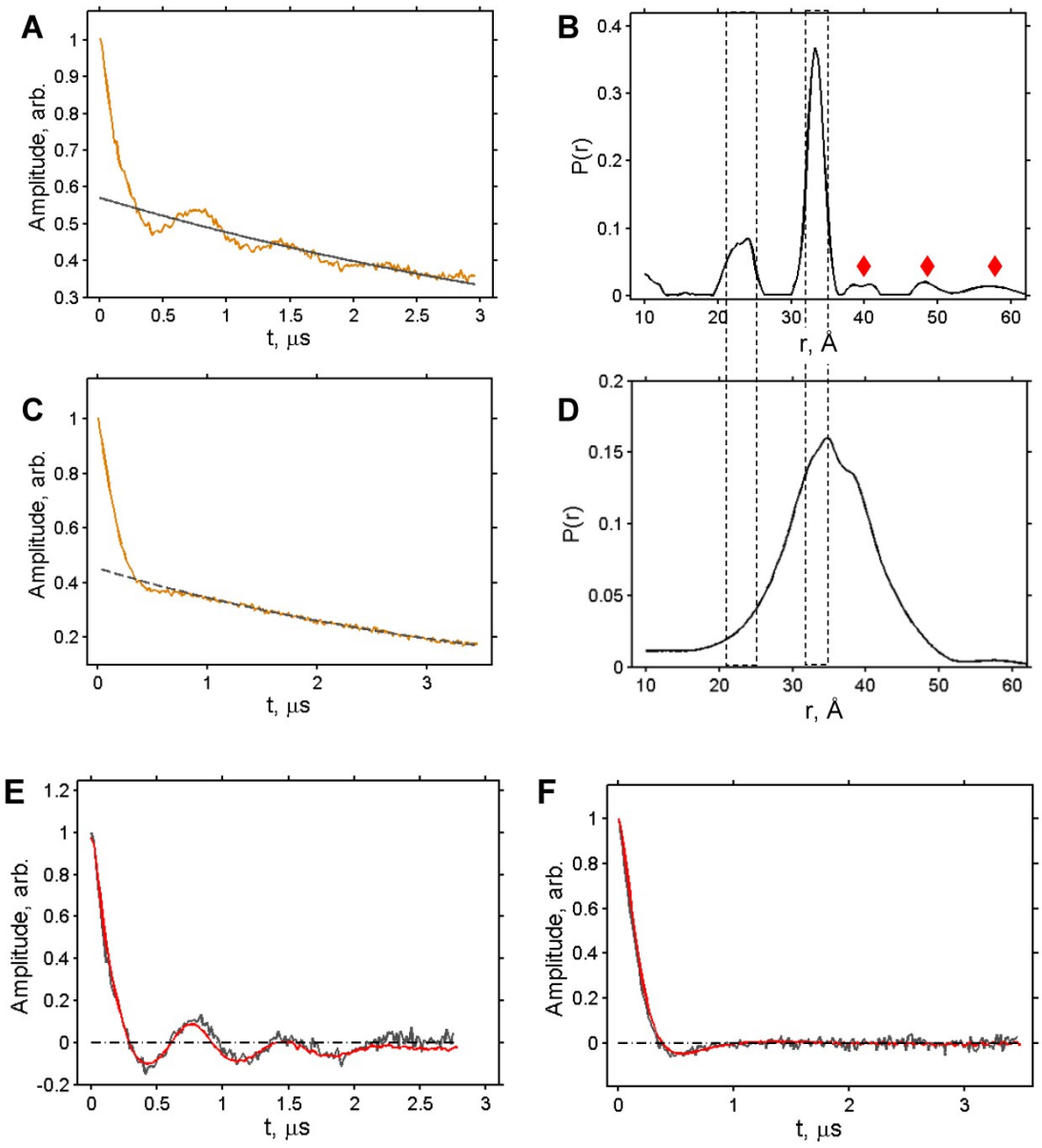

Figure S8. Time-domain raw DEER data from Cu-NO experiments: (**A, B**) is for 150 μM V94R1 and (**C, D**) for 350 μM V94R1:I149T. Clear dipolar oscillations in A and two well-resolved distances in B are no longer observed in C and D. There is large broadening of distribution in D and modulation depth increases to the level exceeding that possible for two coupled nitroxides. (**E, F**) are the fits, (cf. comments in the Fig. S7 caption).

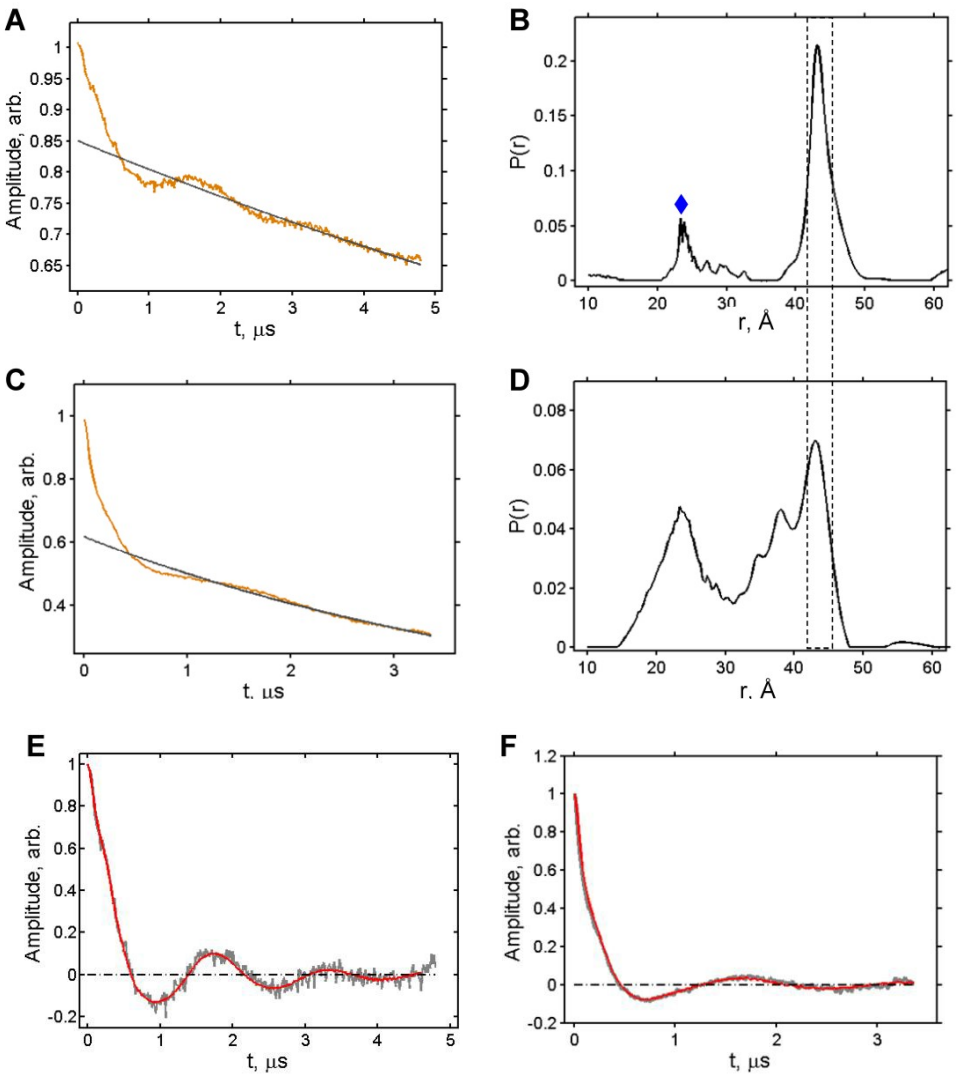

Figure S9. DEER data from NO-NO experiment: (**A, B**) is the case of 150 μM V94R1 and (**C, D**) is for 350 μM V94R1:I149T. In C there is strong damping of oscillations as well as much increased content of short distances and greater modulation depth exceeding the maximum for a pair of nitroxides. Note that in A (and only for this data set) a weak 4 MHz nuclear modulation (ESEEM) from solvent deuterons is present, giving rise to a small-volume peak in B denoted by blue diamond. (This gives a narrow unwanted 23 Å peak in Fig. 3C of the main text.) (**E, F**) are comparisons of background-free data from A and C with time-domain fits based on *P*(*r*)'s in B and D. (No multi-spin effects were included in the fits.)

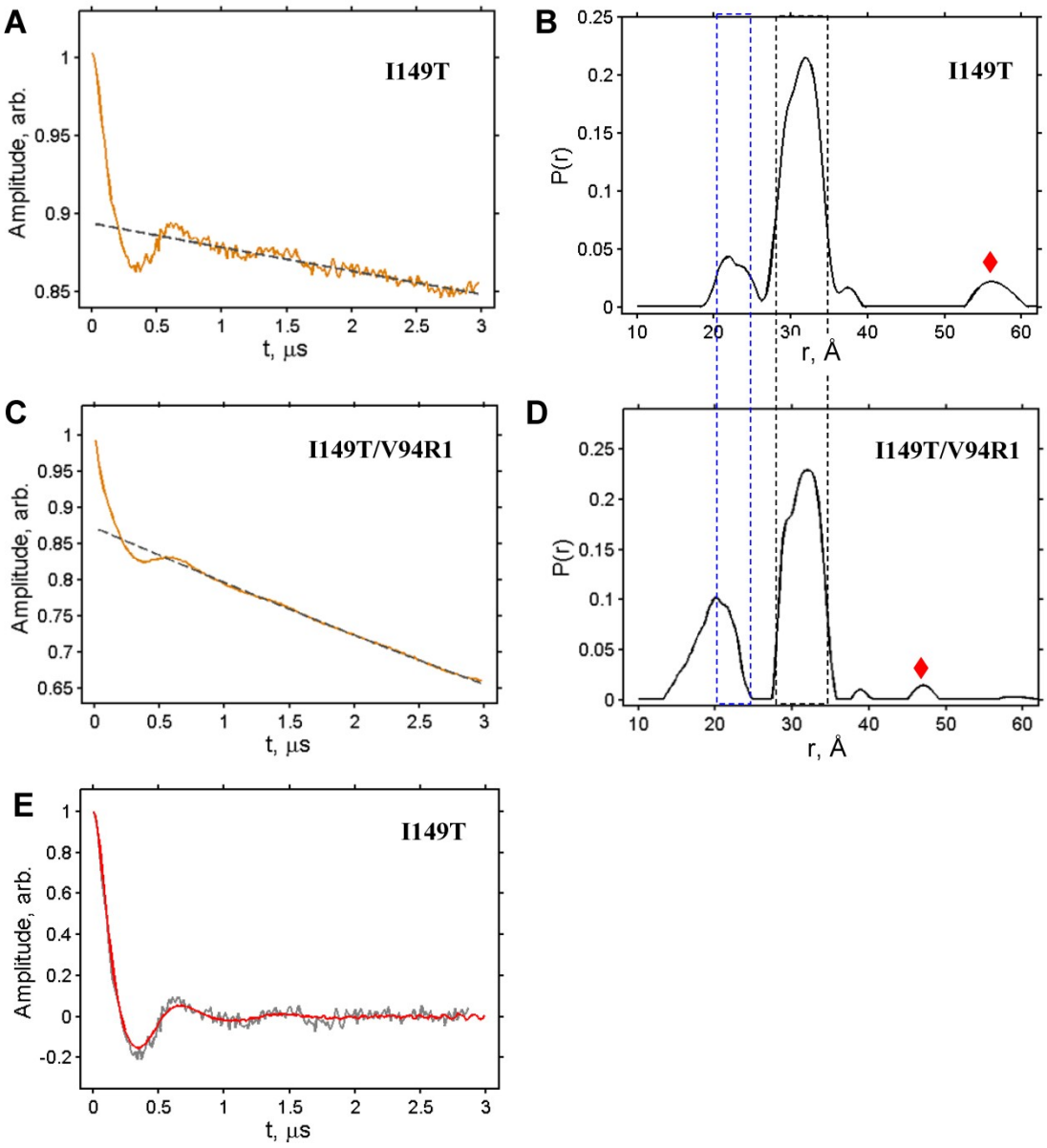

Figure S10. (**A, B**) The DEER data from control Cu-Cu experiment carried out on 350 μM I149T mutant of AS-SOD1. (**C**, **D**) Time-domain DEER data and *P*(*r*) for the case of V94R1:I194T from Fig. S7 are shown for comparison with *P*(*r*) in B. They are different in magnitude of short-distance component, indicating that modification V94R1 further contributes to I149T destabilization of the protein leading to increase of aggregation. (**E**) The fit to the baseline-free data from A based on distributions in B.

C. Structure Modeling and Assessment of SOD1 Aggregation

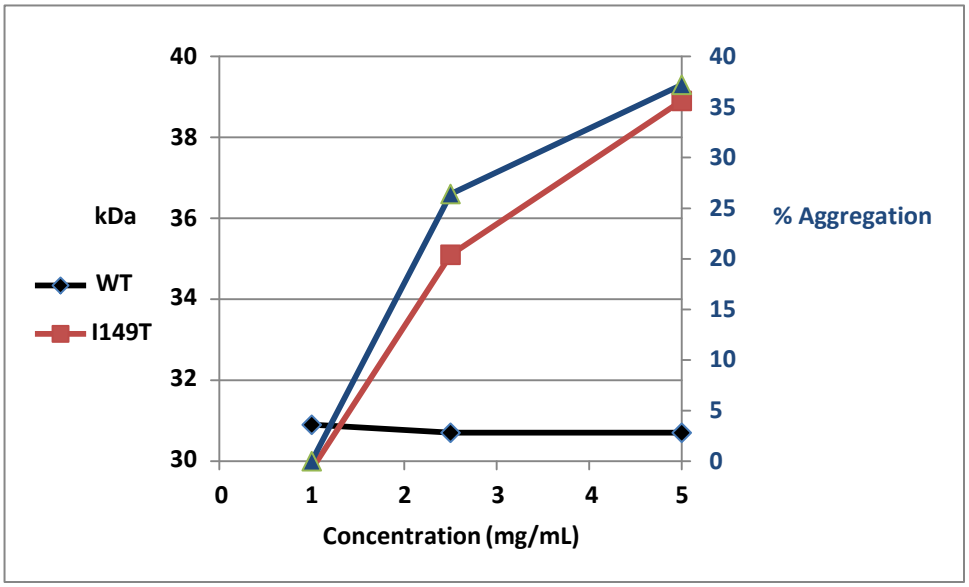

Figure S11. MALS data shows that the I149T mutant undergoes concentration dependent aggregation, which is completely absent for the WT. The black and red traces show average molecular weights for WT and I149T respectively. The blue trace shows the percentage of aggregation in the I149T samples**.**

.

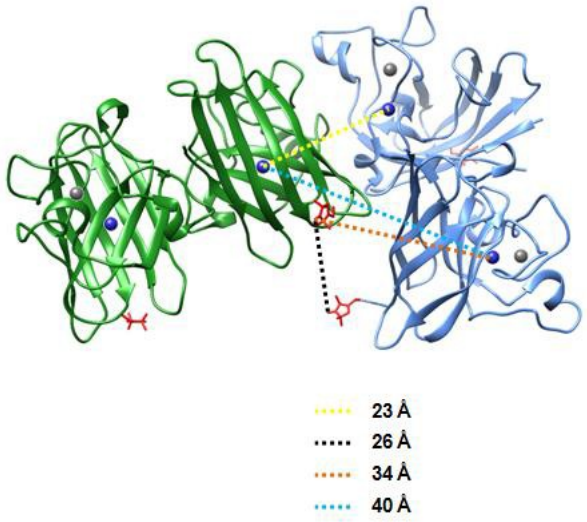

Figure S12. One possible model of the close contact between two I149T dimers (green and blue) based on one of several lattice contacts in the I149T SOD1 crystal. Inter-dimer distances are shown with dashed lines. The interdimer Cu-Cu distance in the crystal lattice agrees well with the new short distance found in I149T by PDS, but rotation about this Cu-Cu axis is required to bring the nitroxide moieties into reasonable agreement with the PDS data (cf. Fig. S13).

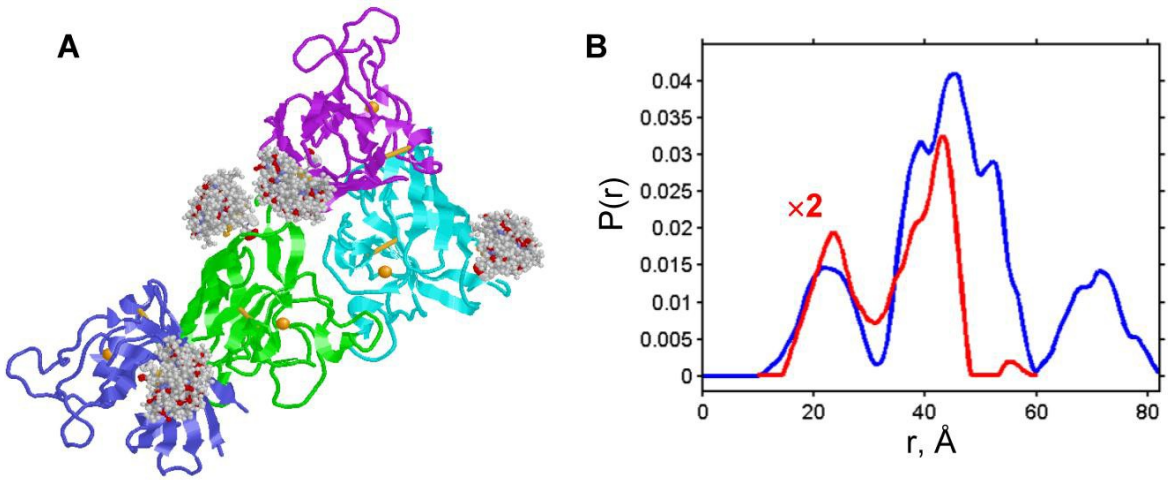

Figure S13. (**A**) R1 side-chain modeling was carried out on the crystal structure of Fig, S12. R1 conformers were simulated using rotamer implemented in MMM2013 (Molecular Multiscale Modeling, software package (12)). (**B**) Distance distributions obtained by rotamer modeling (blue) are compared to the NO-NO experiment on V94R1:I149T (red). As expected, the experimental solution DEER data indicate that the structure must deviate from those suggested by contacts found in the crystal lattice. However, a relatively small restructuring, as noted under Fig. S12, can easily bring all distances into the proper range.

Supporting References:

1. Borbat, P. P., and Freed, J. H. (2007) Measuring Distances by Pulsed Dipolar ESR Spectroscopy: Spin-labeled Histidine Kinases, In *Methods Enzymol* 243: 52-116 (Simon, M. L., Crane, B., and Crane, A., Eds.) 2007/07/05 ed., Academic Press, San Diego.
2. Borbat, P. P., and Freed, J. H. (2014) Pulse dipolar ESR: distance measurements, *Struct. Bond. 152* 1-82. (Harmer, J., and Timmel, C. R., Eds.), DOI 10.1007/430_2012_82, Springer, Berlin, Heidelberg, Germany.
3. Jeschke, G. (2012) DEER Distance Measurements on Proteins, *Annu Rev Phys Chem 63*, 419-446.
4. Borbat, P. P., Crepeau, R. H., and Freed, J. H. (1997) Multifrequency two-dimensional Fourier transform ESR: an X/Ku-band spectrometer, *J Magn Reson 127*, 155-167.
5. Borbat, P. P., Georgieva, E. R., and Freed, J. H. (2013) Improved Sensitivity for Long-Distance Measurements in Biomolecules: Five-Pulse Double Electron-Electron Resonance, *J. Phys. Chem. Lett. 4*, 170-175.
6. Lieberman, R. A., Sands, R. H., and Fee, J. A. (1982) A study of the electron-paramagnetic resonance properties of single monoclinic crystals of bovine superoxide-dismutase, *J. Biol. Chem. 257*, 336-344.
7. Marko, A., Margraf, D., Yu, H., Mu, Y., Stock, G., and Prisner, T. (2009) Molecular orientation studies by pulsed electron-electron double resonance experiments, *J. Chem. Phys. 130*.
8. Ruthstein, S., Ji, M., Mehta, P., Jen-Jacobson, L., and Saxena, S. (2013) Sensitive Cu2+-Cu2+ distance measurements in a protein-DNA complex by double-quantum coherence ESR, *J Phys Chem B 117*, 6227-6230.
9. Borbat, P. P., and Freed, J. H. (1999) Multiple-quantum ESR and distance measurements, *Chem. Phys. Lett. 313*, 145-154.
10. Borbat, P. P., and Freed, J. H. (2000) Distance Measurements in Biological Systems by EPR, In *Biological Magnetic Resonance* (Berliner, L. J., Eaton, G. R., and Eaton, S. S., Eds.), pp 385-459, Academic/Plenum Publishers, New York.
11. Becker, J. S., and Saxena, S. (2005) Double quantum coherence electron spin resonance on coupled Cu(II)-Cu(II) electron spins, *Chem. Phys. Lett. 414*, 248-252.
12. Polyhach, Y., Bordignon, E., and Jeschke, G. (2011) Rotamer libraries of spin labelled cysteines for protein studies, *Phys. Chem. Chem. Phys. 13*, 2356-2366.